Superficial Femoral Artery Stenting: Impact of Stent Design and Overlapping on the Local Hemodynamics

Monika Colombo[1,2], Anna Corti[1], Diego Gallo[3], Andrea Colombo[1], Giacomo Antognoli[1],

Martina Bernini[4], Ciara McKenna[4], Scott Berceli[5,6], Ted Vaughan[4],

Francesco Migliavacca[1], Claudio Chiastra[1,3,*]

1. Laboratory of Biological Structure Mechanics (LaBS), Department of Chemistry, Materials and Chemical Engineering "Giulio Natta", Politecnico di Milano, Milan, Italy
2. Institute for Chemical and Bioengineering, ETH Zurich, Zurich, Switzerland
3. PoliTo[BIO]Med Lab, Department of Mechanical and Aerospace Engineering, Politecnico di Torino, Turin, Italy
4. Biomechanics Research Centre (BioMEC), National University of Ireland Galway, Ireland
5. Department of Surgery, University of Florida, Gainesville, FL, USA
6. Malcom Randall VAMC, Gainesville, FL, USA

Address for correspondence:
Claudio Chiastra, PhD
PoliTo[BIO]Med Lab
Department of Mechanical and Aerospace Engineering
Politecnico di Torino
Corso Duca degli Abruzzi, 24
10129 Turin, Italy
E-mail: claudio.chiastra@polito.it
ORCID: http://orcid.org/0000-0003-2070-6142

Abstract

Background. Superficial femoral arteries (SFAs) treated with self-expanding stents are widely affected by in-stent restenosis (ISR), especially in case of long lesions and multiple overlapping devices. The altered hemodynamics provoked by the stent is considered as a promoting factor of ISR. In this context, this work aims to analyze the impact of stent design and stent overlapping on patient-specific SFA hemodynamics.

Methods. Through a morphing technique, single or multiple stents were virtually implanted within two patient-specific, post-operative SFA models reconstructed from computed tomography. The stented domains were used to perform computational fluid dynamics simulations, quantifying wall shear stress (WSS) based descriptors including time-averaged WSS (TAWSS), oscillatory shear index (OSI), transverse WSS (transWSS), and WSS ratio (WSS$_{RATIO}$). Four stent designs (three laser-cut – EverFlex, Zilver and S.M.A.R.T. – and one prototype braided stent), and three typical clinical scenarios accounting for different order of stent implantation and overlapping length were compared.

Results. The main hemodynamic differences were found between the two main types of stent designs. The braided stent presented lower median transWSS and higher median WSS$_{RATIO}$ than the laser-cut stents (p<0.0001). The laser-cut stents presented comparable WSS-based descriptor values, except for the Zilver, exhibiting a median TAWSS ~30% higher than the other stents. Stent overlapping provokes an abrupt alteration of the WSS-based descriptors. The overlapping length, rather than the order of stent implantation, highly and negatively impacted the hemodynamics.

Conclusion. The proposed computational workflow compared different SFA stent designs and stent overlapping configurations, highlighting those providing the most favorable hemodynamic conditions.

1 Introduction

Peripheral artery disease (PAD) is the main vascular pathology affecting the lower limbs vessels [1], including the superficial femoral artery (SFA), where almost 50% of the atherosclerotic lesions occur [2]. Among the endovascular treatments, the implantation of self-expanding Nitinol stents is one of the most widespread approaches [3]. Two main classes of self-expanding stents are adopted for the femoral region: (i) laser-cut stents, which are characterized by a wide variety of features like strut shape, thickness, length, and width, and interconnecting segments (or links); and (ii) wire braided stents, characterized by sets of interlacing wires running in clockwise and counterclockwise directions [4,5].

The unique extension and characteristics of SFA lesions, frequently longer than 150 mm and presenting with severe calcifications, often require the deployment of multiple long and overlapping stents [6,7]. However, the placement of overlapping stents in SFAs is thought to be associated with worse clinical outcomes compared to the single device strategy, regardless of the stent type, as occurring for other vascular regions [8]. One of the most challenging aspects (also concerning the single stenting therapy) is maintaining long-term patency after revascularization [9], which is limited by in-stent restenosis (ISR) in more than 30% of the cases [10].

In addition to systemic (e.g. age, sex, diabetes, smoking, cardiovascular diseases) and biological (e.g., gene regulatory network) factors, ISR seems to be promoted by biomechanical factors [11]. Specifically, the altered hemodynamics immediately after stenting and during the entire post-operative period has been identified as a concurrent driver of ISR. As previously demonstrated, the physiology of the arterial wall is modulated by low and oscillatory wall shear stress (WSS), which specifically up-regulate the pro-inflammatory vascular responses through mechano-transduction pathways [12,13]. In the case of stenting, in the immediate post-

4

implantation period the stent struts cause local flow disturbances with flow separation and recirculation zones downstream of the struts [14]. Overall, lower WSS values characterize the stented region as compared to a non-treated healthy segment [14]. Focusing on femoral arteries, recent works have demonstrated that WSS, investigated through computational fluid dynamics (CFD) simulations and quantified through different WSS-based descriptors, contributes to the onset and progression of ISR in human stented SFAs [15–17]. Indeed, during ISR progression, the arterial wall undergoes a remodeling process, with changes in WSS that, in turn, modulate the neointima response [18].

The magnitude of the flow disruptions provoked by a stent is mainly dependent on its design [18]. Furthermore, stent overlapping regions (with associated stent strut malapposition) can exacerbate alterations in the hemodynamic environment. While recent CFD works on patient-specific stented SFAs have examined the relationship between the post-procedural hemodynamics and ISR [15–17], a comparative hemodynamic analysis of the different stent designs and overlapping configurations in the context of the SFA is still lacking. Accordingly, the aim of the present work is to assess the impact of (i) stent design and (ii) stent overlapping on the SFA hemodynamics. CFD simulations are performed in patient-specific SFA anatomies comparing different laser-cut and braided stents, and different stent overlapping configurations.

5

2 Material and methods

2.1 Stented SFA models and investigated scenarios

2.1.1 Clinical data

Two SFA lesions (A and B) of two different patients suffering from PAD and treated with stenting at Malcolm Randall VA Medical Center (Gainesville, FL, USA) were considered. The lesions, also analyzed in previous studies [16,17], were treated with the EverFlex stent (EV3, Medtronic, Dublin, Ireland), which is a self-expanding, laser-cut Nitinol device. In particular, in lesion A, a single EverFlex stent (nominal diameter of 6.0 mm, length of 60 mm) was deployed, while two EverFlex stents (nominal diameters of 6.0 mm, lengths of 100 mm) were implanted in lesions B with an overlapping length of ~12 mm. Computed tomography (CT) and Doppler ultrasound (DUS) images were acquired at 1-week follow-up. The study was conducted in accordance with the ethical standards of the institutional review board at University of Florida (Gainesville, FL, USA), and with the 1964 Helsinki Declaration and its later amendments. Informed consent was obtained from the patients.

2.1.2 Three-dimensional vessel reconstruction

The SFA lumen geometry of the two lesions under investigation was obtained from CT scans by employing an in-house three-dimensional (3D) reconstruction method (Fig. 1A) [19]. The common femoral artery bifurcation and the proximal segment of the profunda femoral artery were considered into the vessel reconstruction to take into account their impact on the hemodynamics. Initially, the SFA lumen, visible through injected contrast agent, was segmented slice after slice using an active contour method, based on a level set algorithm [19]. Then, an

6

automatic correction phase was run, in which the initial raw image mask was polished from background noise and calcifications in the non-stented portion, and from the metallic artefacts in the stented region [19].

Due to the low CT resolution (~1 mm) and metallic artefacts, the stents appeared in the CT slices as a bright annulus with a thickness of ~2 mm. The stent struts were not discernible. Nevertheless, the location of the stents and of the stent overlapping region was retrievable by visual inspection (Fig. 1A).
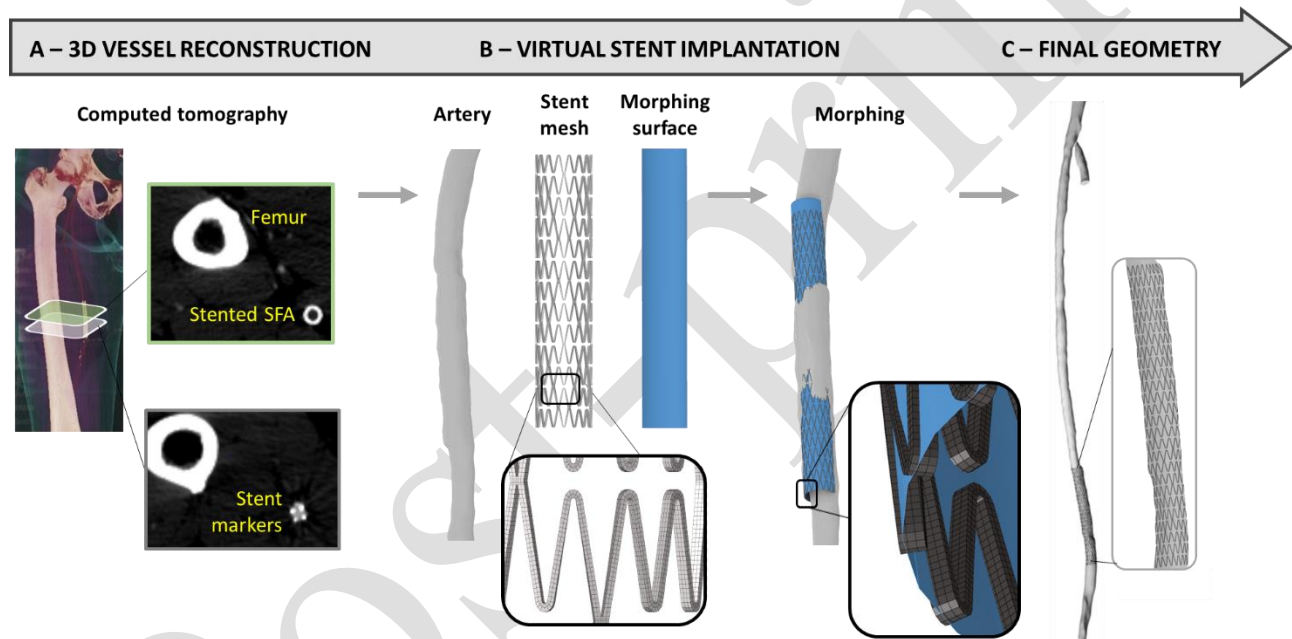

Fig. 1 - Workflow for the creation of the stented superficial femoral artery (SFA) geometries. **A)** Three-dimensional (3D) vessel reconstruction from computed tomography images based on the methodology explained in [19]. **B)** Virtual implantation of the stent inside the vessel geometry using a morphing procedure. The finite element mesh of the stent in its straight configuration is morphed and adapted to the vessel geometry through a morphing surface (hollow cylinder). The stent is properly oriented based on the stent markers visible on computed tomography. **C)** Final stented vessel geometry.

2.1.3 Virtual stent implantation

Given the inability of the CT scan to detect the stent struts, a virtual stent implantation procedure was applied to obtain the stented SFA geometry. The procedure morphed the finite element mesh of the stent from an undeformed straight configuration to a mesh that followed the target vessel geometry. The mesh manipulation tool HyperMorph, available in the software HyperMesh (v. 17, Altair Engineering, Troy, MI, USA), was used as it allowed a robust and quick modification of the stent shape, guaranteeing a minimum mesh element distortion. To perform the stent morphing, the following three components were needed (Fig. 1B): (i) the undeformed stent mesh; (ii) the SFA lumen geometry as target surface destination; and (iii) a cylindrical surface, coaxial with the stent and intersecting the most external element layer of the stent mesh, which was utilized to guide the stent morphing. The undeformed stent mesh and the cylindrical surface were initially positioned along the SFA centerline (Fig. 1B). The axial location of the stent and, if present, of the stent overlapping region was retrieved from the CT images. Moreover, the angular position of the stent around the SFA main axis was defined according to the markers visible on CT at the stent extremities (Fig. 1A). Then, the morphing domain, consisting of the stent nodes to be morphed on the destination luminal surface, was created. Finally, the software elaborated the nodal transformation providing the deformed stent mesh and the resultant stented SFA geometry (Fig. 1C). To allow a more realistic stent deployment and apposition to the vessel wall, a penetration depth of 20% of the strut thickness was imposed. The use of a cylindrical surface to guide the morphing procedure allowed a perfect adhesion of the deployed stent onto the irregular geometry and a reduction of the mesh element distortion. In the case of overlapping stents, once the first stent model was virtually implanted using the procedure described above, a surface tangent to the internal elements of the first stent

model was added at the overlapping region in order to correctly position the second stent model (Supplementary Fig. S1).

2.1.4 Investigated scenarios

Lesion A was employed to analyze the impact of the stent design on SFA hemodynamics. In particular, the following four self-expanding Nitinol devices were compared from the hemodynamic viewpoint (Fig. 2): the commercial laser-cut (i) EverFlex (EV3, Medtronic); (ii) Zilver PTX (Cook Medical, Bloomington, IN, USA); (iii) S.M.A.R.T. Vascular System (S.M.A.R.T., Santa Clara, CA, USA) stents; and (iv) a prototype wire braided stent [20]. The three laser-cut stents consist of repetitive rings, connected through links of different shapes and characterized by rectangular cross-section of different size (detailed in Fig. 2). Meanwhile, the wire, braided stent is made from 24 crossing/weaved wires wrapped on itself in a helical manner, with circular cross-section, woven at a braid angle of 30°, defined as the angle between the radial axis and the direction of the wires (as illustrated in Fig. 2) [4]. Further details of the cells of the laser-cut and braided stents are reported in Table 1. The 3D models of the stents were created with SolidWorks (v.2020, Dassault Systèmes, Vélizy-Villacoublay, France) considering a nominal diameter of 6 mm and a length of 60 mm.
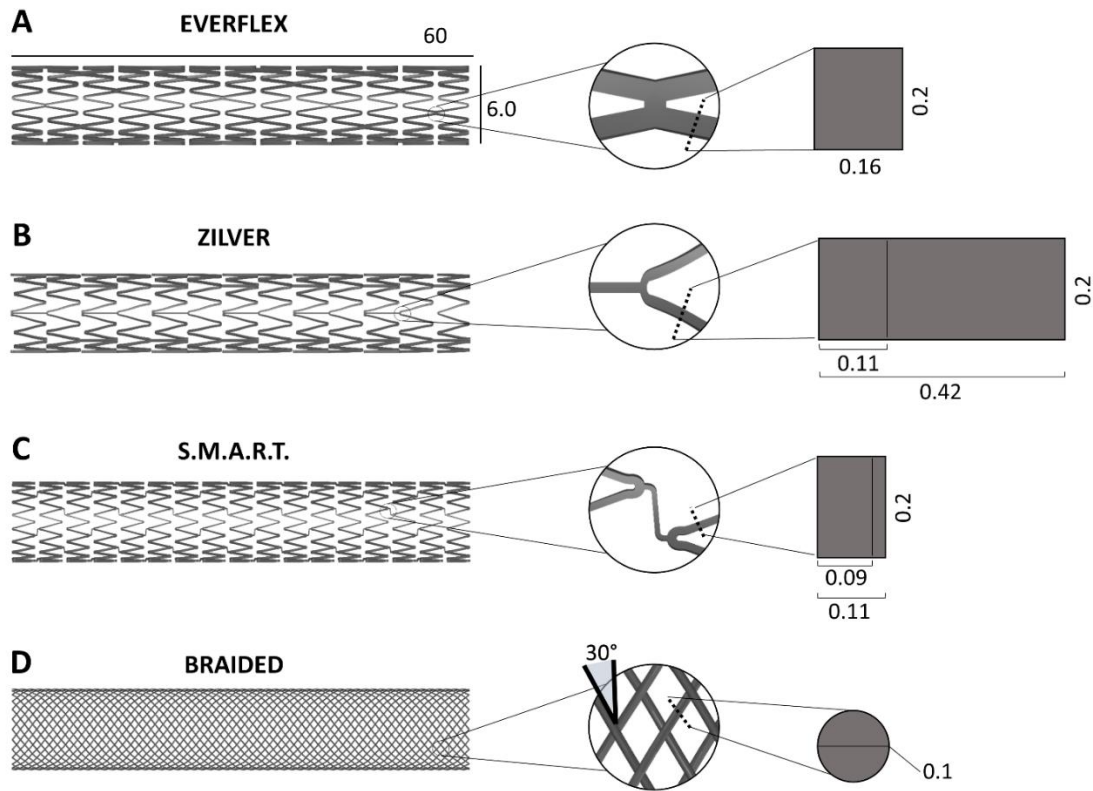
Fig. 2 - Self-expanding Nitinol stents compared from the hemodynamic viewpoint: **A)** EverFlex (EV3, Medtronic), **B)** Zilver PTX (Cook Medical, Bloomington, IN, USA), and **C)** S.M.A.R.T. Vascular System (S.M.A.R.T., Santa Clara, CA, USA) laser-cut stents; **D)** prototype braided stent (with a detail of the braid angle of 30 °). On the right, a detail of the link between two rings for the laser-cut devices and of the three-dimensional wired structure of the braided stent, with a schematic cross-section. Zilver and S.M.A.R.T. stents present a variable strut width, and the minimum and maximum dimensions are illustrated. Dimensions are presented in [mm].

Table 1. Main characteristics of the investigated stents for the treatment of femoral arteries.

	Strut length [mm]	Number of struts	Cell area (total cell area) [mm²]	Strut cross-section [mm²]	Thickness [mm]
EverFlex	2.3	26	1.95 (810.2)	Constant regular 0.032	0.2
Zilver	2.4	25	9.35 (972.0)	Variable rectangular 0.023-0.084	0.2
S.M.A.R.T.	1.8	33	4.77 (972.6)	Variable rectangular 0.018-0.022	0.2
Braided	1.1	55	0.79 (1066.1)	Constant circular 0.008	0.1

10

Lesion B was employed to analyze the impact of the interventional procedure, in case of multiple stent deployments and considering the order of stent implantation and of overlapping length on SFA hemodynamics. In the clinical routine, in presence of long lesions requiring the implantation of at least two stents, the distal device may be deployed first, followed by the proximal one. This configuration was here virtually replicated and referred to as "step-down", due to the path followed by the blood flow (Fig. 3A). Furthermore, two additional configurations were analyzed, namely the "step-up" configuration (Fig. 3A), in which the stents are implanted in the opposite order (i.e. first the proximal stent, second the distal one), and the "long-overlap" configuration (Fig. 3B), in which the stents are implanted in the step-down configuration but resulting in a longer overlapping region. In the case of the step-up and step-down configurations, a proximal 6.0x120 mm EverFlex stent and distal 6.0x100 mm EverFlex stent were virtually implanted (same stent size of the real scenario), resulting in an overlapping length of ~12 mm (net axial distance measured from the CT reconstruction). In the case of the long-overlap configuration, a proximal 6.0x150 mm EverFlex stent (larger size of the device, as reported in the Medtronic Peripheral U.S. Product Catalog of 2021) was virtually placed, resulting in an overlapping length of ~32 mm.
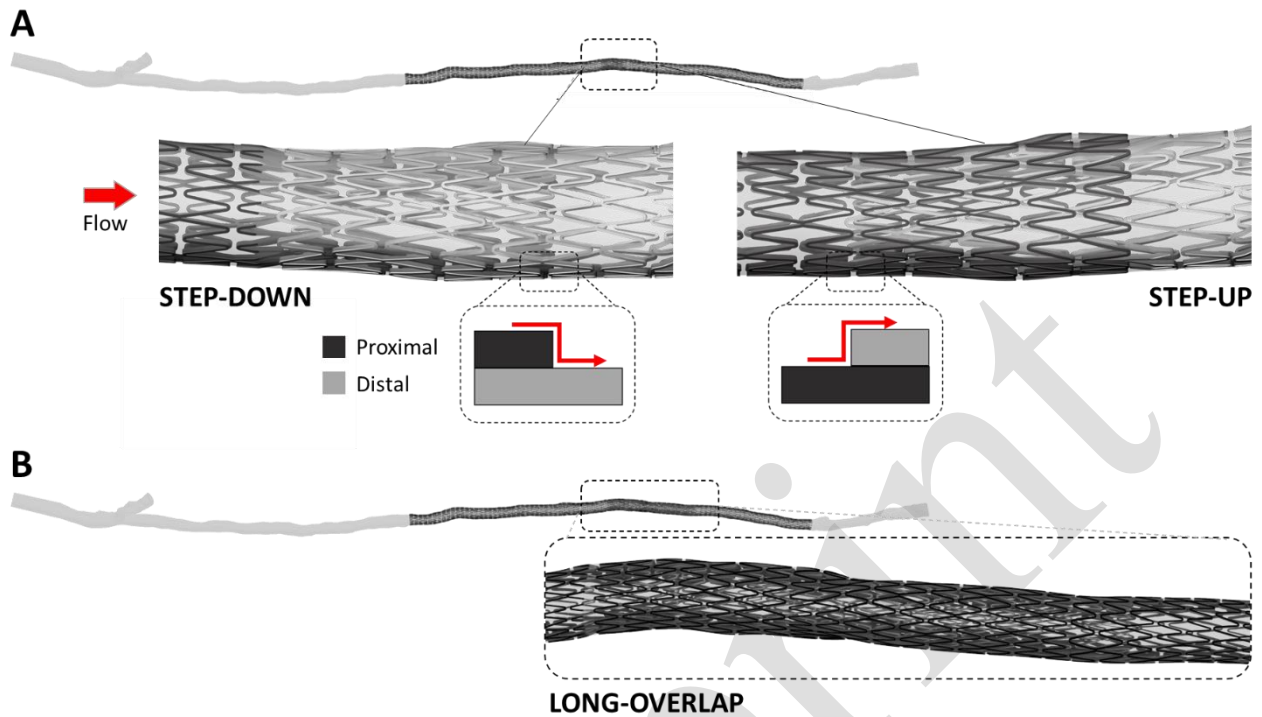
11

Fig. 3 - **A)** Vessel models with short stent overlapping length (~12 mm): on the left, the step-down configuration, in which the distal stent is implanted first and the proximal one second; on the right, the step-up configuration, in which the stents are implanted in the opposite order. **B)** Vessel model with long stent overlapping length (~32 mm): long-overlap configuration, in which the stents are implanted in the step-down fashion. In each case, two EverFlex stents were virtually implanted in lesion B.

2.2 Computational fluid dynamics

2.2.1 Meshing

The geometry of the stented arteries was discretized using Fluent Meshing (v.18.2, Ansys Inc., Canonsburg, PA, USA). Tetrahedral meshes with five prism layers close to the luminal surface and smaller elements in the vicinity of the stent struts were created (Fig. 4A). A mesh independence study was carried out on the case of lesion A treated with EverFlex device and

mesh cardinalities ranging from 3,945,149 to 15,064,181 elements were considered. Taking the latter as reference, the best compromise in terms of computational effort and accuracy (differences lower than 3 % in the stented region and lower than 1.5 % in the non-stented portions in terms of mean TAWSS and transWSS) resulted in a minimum element size of 0.008 mm and a boundary layer with an exponential growth rate of 1.1 and a total height of 0.05 mm. The resulting mesh cardinalities for the cases under investigation ranged from 7,455,156 (Zilver stent) to 15,094,693 (braided stent) elements for lesion A, and from 23,279,404 (step-down) to 26,168,217 (long-overlap) elements for lesion B.
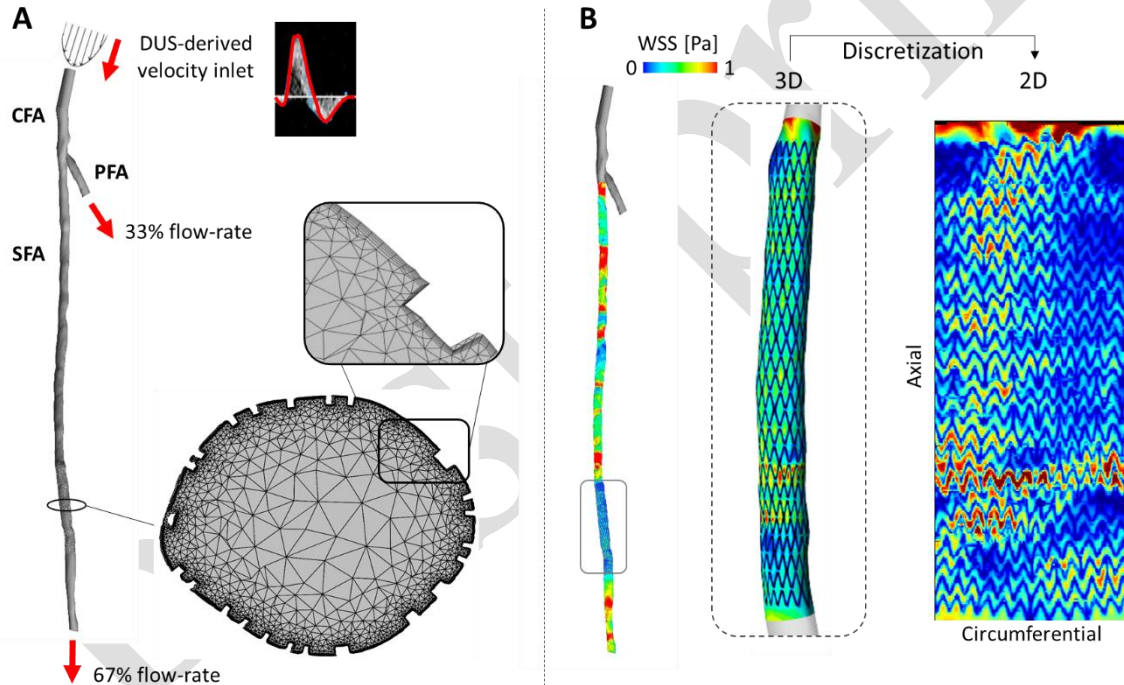

Fig. 4 - Computational fluid dynamics (CFD) model of lesion A treated with the EverFlex stent. **A)** Boundary conditions and details of the computational grid of a cross-section of the stented portion. **B)** Example of the transformation of a three-dimensional (3D) map of wall shear stress (WSS) obtained from the CFD simulation into the corresponding two-dimensional (2D) map. CFA: common femoral artery; FPA: profunda femoris artery; SFA: superficial femoral artery.

13

2.2.2 Simulations

Transient, laminar CFD simulations were performed using Fluent (v.18.2, Ansys Inc.). Based on our previous work [19], a patient-specific parabolic velocity profile derived from the velocity waveform extracted from patients' DUS images was imposed at the common femoral artery inlet (highlighted in red in Fig. 4A). The peak velocities derived from the Doppler spectrum were processed through the algorithm proposed in [21]. A flow-split of 0.67:0.33 was imposed at the SFA and profunda femoral artery outlets, respectively. The no-slip condition was applied to the walls, assumed as rigid. The blood was modeled as a non-Newtonian Carreau fluid with constant density of $1060\,kg/m^3$. According to a previous sensitivity analysis [18], two cardiac cycles of 100 time steps each were simulated and were sufficient to provide accurate hemodynamic results. The duration of the cardiac cycles, derived from the DUS images, were 1.03 and 0.91 seconds for lesions A and B, respectively. The solver settings are summarized in Table 2.

Table 2. Computational fluid dynamics solver settings.

Type	Pressure-based (Ansys Fluent)
Pressure-velocity coupling method	Coupled
Spatial discretization scheme	
Gradient	Least squares cell based
Pressure	Second order
Momentum	Second order upwind
Transient formulation	Second order implicit
Relaxation factors	
Fluent flow courant number	50
Explicit relaxation factors	
Momentum	0.35
Pressure	0.35
Residual value for convergence	
Continuity	$5\cdot10^{-5}$
Velocity	$5\cdot10^{-5}$

2.3 Post-processing and statistical analyses

2.3.1 Hemodynamic descriptors' quantification

The local hemodynamics along the stented region was analyzed by computing several WSS-based descriptors, quantifying the magnitude, the oscillatory and multidirectional nature of the WSS vector field over the cardiac cycle. The list of the computed indexes, as well as their mathematical definition and explanation, is reported in Table 3.

Table 3 – Wall shear stress (WSS) based descriptors computed in the study.

WSS-based descriptor	Mathematical definition	Explanation
Time-averaged WSS	$\text{TAWSS} = \dfrac{1}{T} \int_0^T |\textbf{WSS}| \, dt$	Cardiac cycle-average WSS vector magnitude
Oscillatory shear index	$\text{OSI} = 0.5 \left[1 - \left(\dfrac{\left| \int_0^T \textbf{WSS} \, dt \right|}{\int_0^T |\textbf{WSS}| \, dt} \right) \right]$	Index ranging between 0 and 0.5 quantifying oscillations in the WSS direction during the cardiac cycle [22]
Relative residence time	$\text{RRT} = \dfrac{1}{\text{TAWSS} \cdot (1 - 2 \cdot \text{OSI})} = \dfrac{1}{\frac{1}{T} \left| \int_0^T \textbf{WSS} \, dt \right|}$	Index inversely proportional to the magnitude of the time-averaged WSS vector. Defined as a combination of TAWSS and OSI [23]
Transverse WSS	$\text{transWSS} = \dfrac{1}{T} \int_0^T \left| \textbf{WSS} \cdot \left(\textbf{n} \times \dfrac{\int_0^T \textbf{WSS} \, dt}{\left| \int_0^T \textbf{WSS} \, dt \right|} \right) \right| dt$	Cardiac cycle-average of the WSS component normal to the direction of the time-averaged WSS vector [24]
Cross flow index	$\text{CFI} = \dfrac{1}{T} \int_0^T \left| \dfrac{\textbf{WSS}}{|\textbf{WSS}|} \cdot \left(\textbf{n} \times \dfrac{\int_0^T \textbf{WSS} \, dt}{\left| \int_0^T \textbf{WSS} \, dt \right|} \right) \right| dt$	Normalized transWSS [24]
Time-averaged WSS$_{ax}$ magnitude	$\text{TAWSSax} = \dfrac{1}{T} \int_0^T |\textbf{WSS}_{ax}| \, dt$	Cardiac cycle-average of the WSS component aligned with the tangent to the vessel centerline [25]
Time-averaged WSS$_{sc}$ magnitude	$\text{TAWSSsc} = \dfrac{1}{T} \int_0^T |\textbf{WSS}_{sc}| \, dt$	Cardiac cycle-average of the WSS component aligned with the secondary direction (i.e. orthogonal to the vessel centerline tangent) [25]
WSS ratio	$\text{WSS}_{ratio} = \dfrac{1}{T} \int_0^T \dfrac{|\textbf{WSS}_{sc}|}{|\textbf{WSS}_{ax}|} \, dt$	Ratio between the cardiac cycle-average magnitude of the secondary and axial WSS components [25]

WSS is the WSS vector; T is the period of the cardiac cycle; t is the time; **n** is the unit vector normal to the luminal surface at each element of the mesh.

15

To post-process the hemodynamic results, the 3D WSS distributions along the stented luminal region obtained from the CFD simulations were transformed into two-dimensional (2D) maps (Fig. 4B) [26]. More in detail, the vessel centerline attributes were extracted for each node of the 3D surface meshes using the Vascular Modelling Tool Kit (v.1.3, Orobix, Bergamo, Italy). Then, the WSS data were imported in Matlab (v.R2020a, MathWorks, Natick, MA, USA) where the WSS-based descriptors were computed and represented through 2D color maps. The cell size of the 2D maps was defined through a sensitivity analysis, run on lesion A. In fact, the element number of the initial 3D surface meshes was extremely large (~340,000 surface elements in the smallest case, in the stented portion only) and could widely affect the results of the statistical tests to compare the stent designs and interventional procedures (see Section 2.3.2). Hence, the corresponding 2D cells to be analyzed were reduced to the minimum number still capturing all the local hemodynamic features computed through the initial 3D mesh, with the advantage of more reliable statistical results. To do this, the finest 2D map was created by choosing: (i) the circumferential cell size equal to the minimum size of the 3D mesh elements (0.07 mm); and (ii) the axial cell size in accordance with the proportions of the stented portion of lesion A (~3.2:1 for the length vs. perimeter). Following this method, the finest 2D map consisted of 68,310 cells. Then, the cell size was progressively increased (cell number halved each time) until the percentage difference in terms of mean WSS, and 5th and 95th percentile of the WSS distribution with respect to the finest map remained below 3%. The resulting cell size was 0.42 mm and 1.33 mm in the circumferential and axial directions, respectively. The final cell numbers were 2,025 and 5,850 for lesions A and B, respectively.

2.3.2 Statistical analysis

Data were presented as either mean ± standard deviation or median [interquartile range], depending on the distribution. The normality of the distributions was evaluated using Kolmogorov-Smirnov test. Given the non-normal distributions, the different groups (i.e. four stent designs, three overlapping configurations, and subgroups between non-overlapping and overlapping portions) were compared using analysis of variance or Kruskal-Wallis tests. Then, the individual distributions were tested through Mann-Whitney U test. The statistical analyses were performed using Prism (v.8.3.1, GraphPad Software, San Diego, CA, USA) and Matlab. A two-tailed, p-value < 0.05 was considered as significant.

3 Results

In this section, the hemodynamic results of the impact of stent design (Section 3.1) and of stent overlapping (Section 3.2) are reported in terms of TAWSS, OSI, WSS_{RATIO}, and transWSS, as the most relevant parameters for comparison. The results concerning the other WSS-based descriptors (i.e. RRT, CFI, $TAWSS_{AX}$, and $TAWSS_{SC}$) are presented in the Supplementary Materials for the sake of completeness.

3.1 Impact of stent design

From the qualitative comparison of the 2D maps of the WSS-based descriptors of the four investigated stents (Fig. 5), the major differences in terms of local hemodynamics were observed between the three laser-cut stents and the braided stent. While the TAWSS and OSI color maps for both the laser-cut and braided stents were similar, in the case of transWSS and WSS_{RATIO} the maps presented larger differences. The transWSS was higher for the laser-cut stents compared to

17

the braided one. The WSS$_{RATIO}$ was lower in the case of the laser-cut stents as compared to the braided one, in which larger luminal areas were exposed to WSS$_{RATIO}$ higher than 1, meaning that the local secondary WSS component predominated over the cardiac cycle (Supplementary Fig. S2).
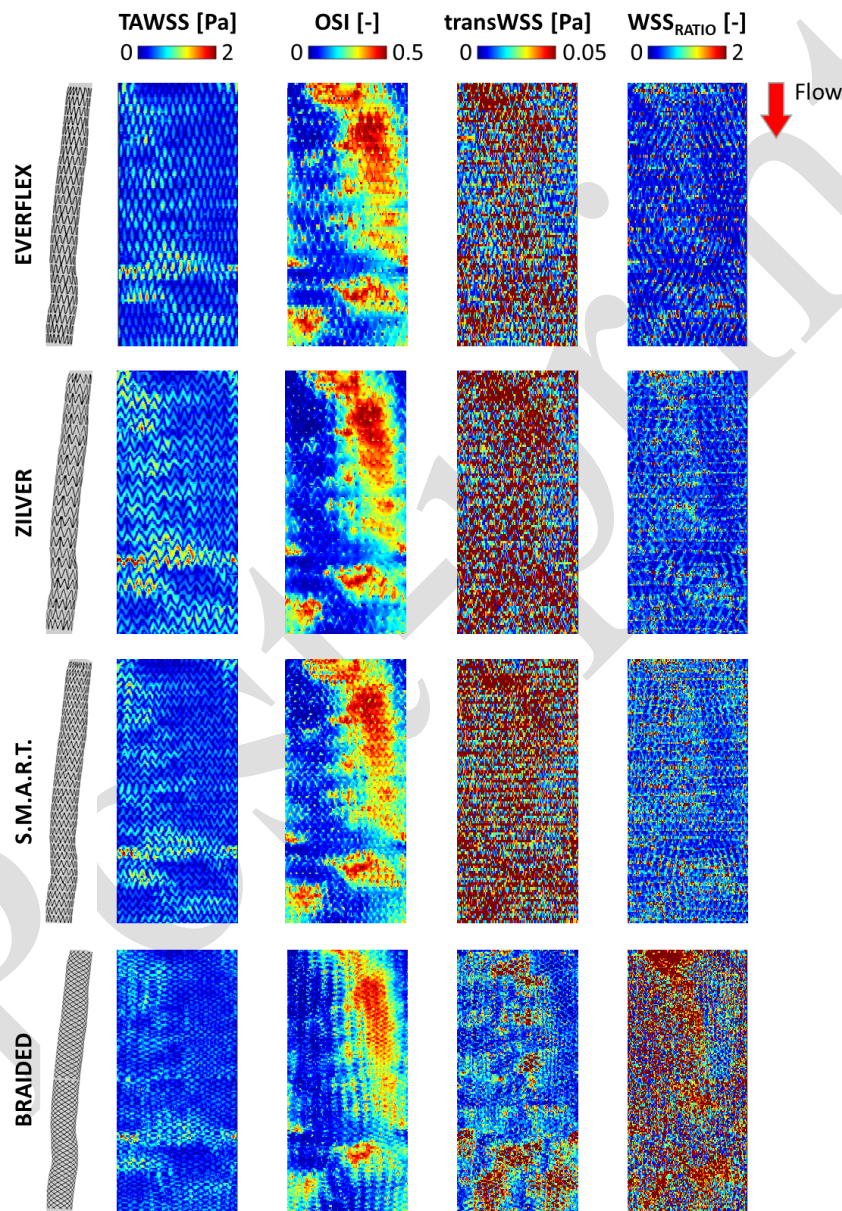

Fig. 5 – Impact of stent design: two-dimensional maps of time-averaged wall shear stress (TAWSS), oscillatory shear index (OSI), transverse WSS (transWSS), and WSS ratio (WSS$_{RATIO}$) for the EverFlex, Zilver, S.M.A.R.T., and braided stents.

These qualitative considerations were supported by the analysis of the distributions of the WSS-based descriptors, visualized as violin plots in Fig. 6A and complemented by the median [interquartile range] values reported in Table 4. The highest TAWSS median value (0.43 [0.23-0.65] Pa) was found in the Zilver stent case. Its TAWSS distribution significantly differed ($p <$ 0.0001) from the other stents, namely from the EverFlex, S.M.A.R.T. and braided stents. The OSI median values, as well as the interquartile range, were similar among the four groups, with the braided stent presenting with the lowest OSI value (EverFlex: 0.19 [0.10-0.31]; Zilver: 0.16 [0.07-0.28]; S.M.A.R.T.: 0.18 [0.09-0.30]; and Braided 0.15 [0.07-0.26]). However, from a statistical viewpoint, the distribution of OSI was significantly different in each group comparison ($p < 0.0001$), probably due to the data sample size affecting the statistical power of the test. The braided stent was characterized by the lowest transWSS median value (0.01 [0.01-0.03] Pa) and the highest WSS_{RATIO} (1.37 [0.65-2.84]), whose value was more than 4-fold that of the EverFlex. Both the transWSS and the WSS_{RATIO} distributions were significantly different in each group comparison (Fig. 6A).

The main results are summarized by the radar chart of Fig. 6B, which displays the median values of the WSS-based descriptors, normalized by the largest median value among the four devices. Overall, from this chart it emerged that the laser-cut stents induced similar local hemodynamic patterns. Instead, the braided stent presented different WSS multidirectional patterns, characterized by lower transWSS and higher WSS_{RATIO} than those of the laser-cut stents (see also Supplementary materials).
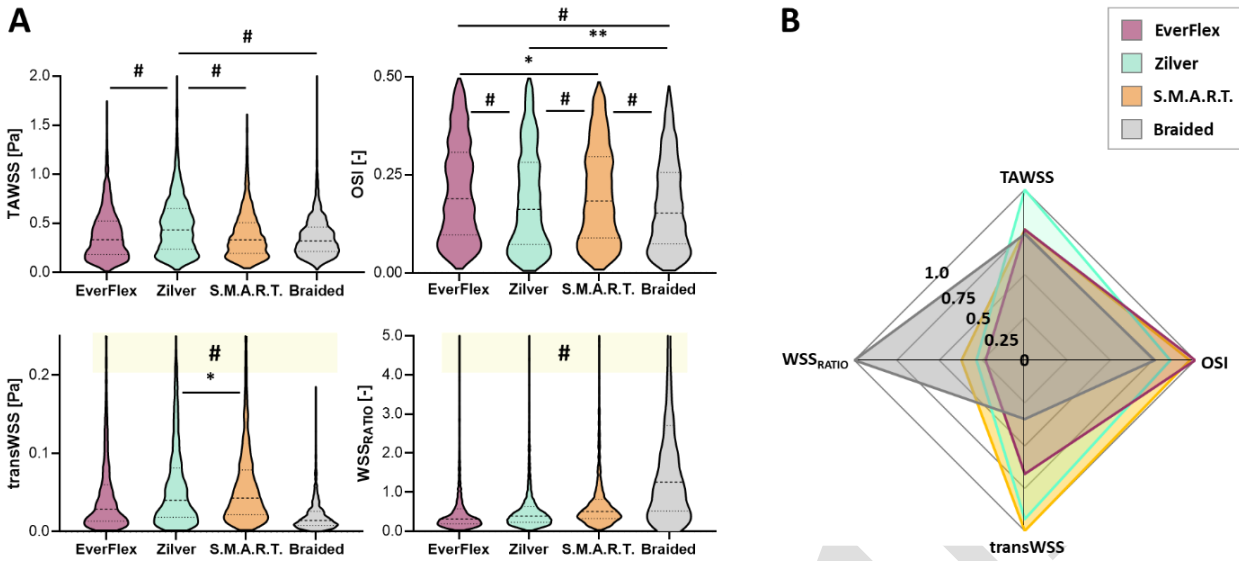
19

Fig. 6 – Impact of stent design: **A)** distributions of time-averaged wall shear stress (TAWSS), oscillatory shear index (OSI), transverse WSS (transWSS), and WSS ratio (WSS$_{RATIO}$) for the EverFlex, Zilver, S.M.A.R.T., and braided stents; in case of transWSS (but Zilver and S.M.A.R.T.) and WSS$_{RATIO}$, each group was significantly different from the others with a p-value lower than 0.0001; **B)** radar chart of the median values of the hemodynamic descriptors for the stents under investigation, each of them normalized by the largest median value among the four devices. *: $p < 0.05$; **: $p < 0.01$; #: $p < 0.0001$.

Table 4 – Impact of stent design: median value and interquartile range (IQR) of the hemodynamic descriptors of each stent design.

STENT DESIGN	EverFlex Median [IQR]	Zilver Median [IQR]	S.M.A.R.T. Median [IQR]	Braided Median [IQR]
TAWSS [Pa]	0.33 [0.18-0.52]	0.43 [0.23-0.65]	0.33 [0.19-0.51]	0.32 [0.21-0.46]
OSI [-]	0.19 [0.10-0.31]	0.16 [0.07-0.28]	0.18 [0.09-0.30]	0.15 [0.07-0.26]
transWSS [Pa]	0.03 [0.01-0.06]	0.04 [0.02-0.08]	0.04 [0.02-0.08]	0.01 [0.01-0.03]
WSS$_{RATIO}$ [-]	0.31 [0.19-0.58]	0.39 [0.23-0.64]	0.51 [0.33-0.82]	1.37 [0.65-2.84]

20

3.2 Impact of stent overlapping

From the qualitative comparison of the 2D maps of the WSS-based descriptors of the three overlapping configurations (Fig. 7), it emerged that the stent overlapping led to changes in the patterns of the WSS-based descriptors (in particular of the TAWSS) as compared to the upstream and downstream stented portions. To confirm this, a quantitative comparison of the distributions of the WSS-based descriptors is shown for the step-down configuration, considered as a representative case (Fig. 8). The distributions of each WSS-based descriptor of the overlapping region were significantly different ($p < 0.0001$) to those of the other portions (Fig. 8), with lower median values of TAWSS and transWSS, and higher median values of OSI and WSS_{RATIO} (Table 5). Conversely, the regions upstream and downstream from the overlapping presented similar median values and distributions of the WSS-based descriptors, with significant differences ($p < 0.0001$) only in the case of TAWSS (0.52 [0.31-0.79] vs. 0.56 [0.34-0.88] Pa for the upstream and downstream stented portions, respectively), and WSS_{RATIO} (0.27 [0.17-0.44] vs. 0.24 [0.16-0.37] for the upstream and downstream stented portions, respectively). Similar findings were found for the step-up and long-overlap configurations (results shown in the Supplementary Materials, Figs. S6 and S7). Moreover, in the overlapping regions of the step-down, step-up, and long-overlap configurations, the distributions of the WSS-based descriptors were statistically identical.
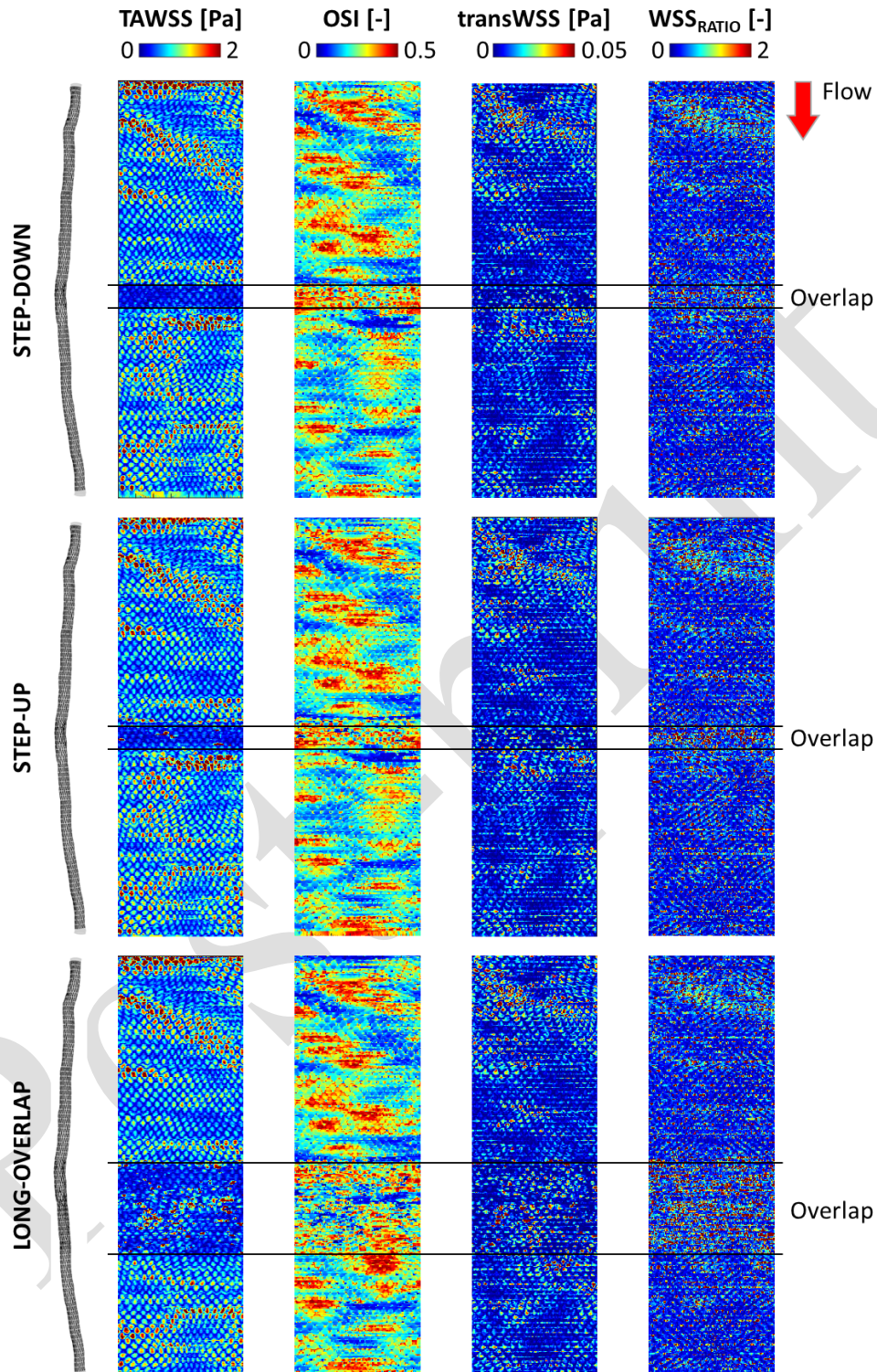
Fig. 7 – Impact of stent overlapping: two-dimensional maps of time-averaged wall shear stress (TAWSS), oscillatory shear index (OSI), transverse WSS (transWSS), and WSS ratio (WSS_{RATIO}) for the step-down, step-up and long-overlap configurations.
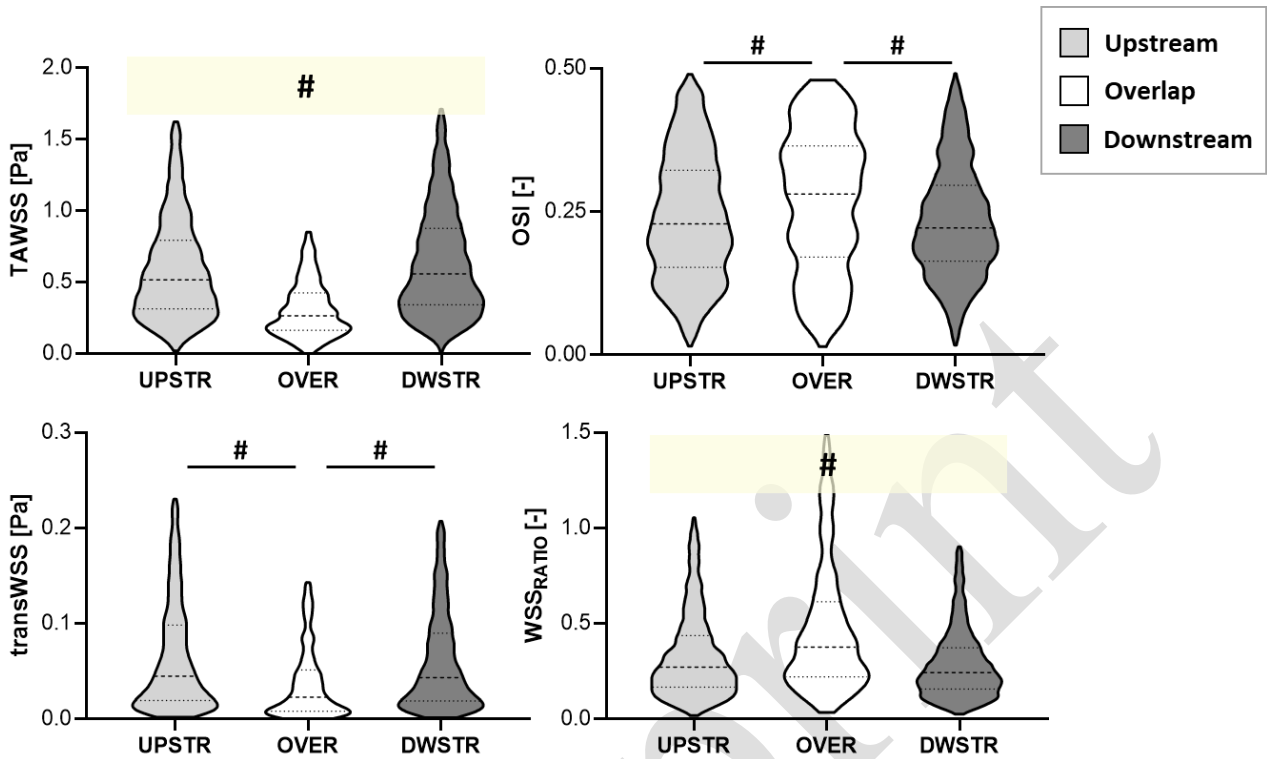
Fig. 8 – Impact of stent overlapping in terms of distributions of time-averaged wall shear stress (TAWSS), oscillatory shear index (OSI), transverse WSS (transWSS), and WSS ratio (WSS_{RATIO}) for the step-down configuration in the overlapping region (OVER) and the portions upstream (UPSTR) and downstream (DWSTR) from the overlapping. #: $p < 0.0001$.

Table 5 – Impact of stent overlapping: median value and interquartile range (IQR) of the hemodynamic descriptors of the overlapping region and the portion upstream and downstream from the overlapping for the step-down configuration.

STENT OVERLAPPING	Upstream Median [IQR]	Overlapping Median [IQR]	Downstream Median [IQR]
TAWSS [Pa]	0.52 [0.31-0.79]	0.26 [0.16-0.42]	0.56 [0.34-0.88]
OSI [-]	0.23 [0.15-0.32]	0.28 [0.17-0.36]	0.22 [0.13-0.30]
transWSS [Pa]	0.04 [0.02-0.10]	0.02 [0.01-0.05]	0.04 [0.02-0.09]
WSS$_{RATIO}$ [-]	0.27 [0.17-0.44]	0.38 [0.22-0.61]	0.24 [0.16-0.37]

The step-down and step-up configurations presented similar local hemodynamic patterns, as visually emerged from the 2D maps of the WSS-based descriptors (Fig. 7). As expected, the long-overlap configuration was characterized by a longer region (overlapping segment) with different hemodynamic patterns. Nevertheless, due to the high number of considered points, significant differences ($p<0.0001$) were found between the distributions of each hemodynamic descriptor of the three configurations under investigation (Fig. 9A). However, by considering only the median values, the long-overlap configuration presented lower median values of TAWSS and higher median values of OSI and WSS_{RATIO} emerged than the other two configurations (Fig. 9B, Table 6).
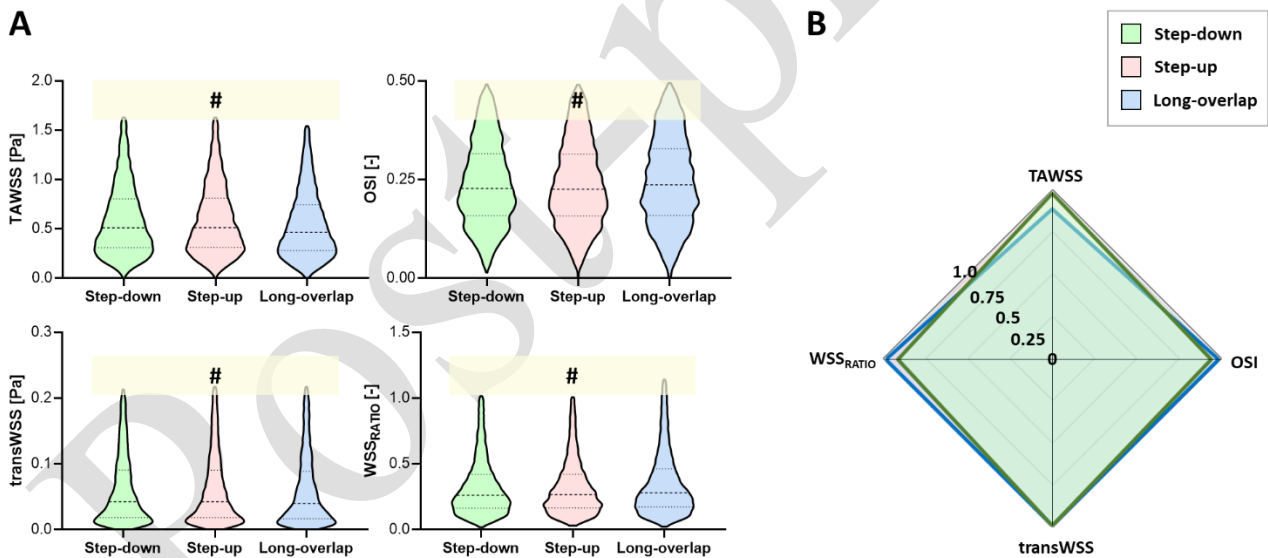

Fig. 9 – Impact of the interventional choice: **A)** distributions of time-averaged wall shear stress (TAWSS), oscillatory shear index (OSI), transverse WSS (transWSS), and WSS ratio (WSS_{RATIO}) for the step-down, step-up and long-overlap configurations; **B)** radar chart of the median values of the hemodynamic descriptors for the configurations under investigation, each of them normalized by the largest median value among the three configurations devices. #: $p < 0.0001$.

Table 6 – Impact of interventional choice: median value and interquartile range (IQR) of the hemodynamic descriptors for each overlapping configuration, considering the total distributions.

INTERVENTIONAL CHOICE	Step-down Median [IQR]	Step-up Median [IQR]	Long-overlap Median [IQR]
TAWSS [Pa]	0.51 [0.31-0.80]	0.51 [0.31-0.81]	0.46 [0.28-0.74]
OSI [-]	0.23 [0.16-0.32]	0.23 [0.16-0.31]	0.24 [0.16-0.33]
transWSS [Pa]	0.04 [0.02-0.09]	0.04 [0.02-0.09]	0.04 [0.02-0.09]
WSS$_{RATIO}$ [-]	0.26 [0.16-0.42]	0.27 [0.16-0.42]	0.28 [0.17-0.46]

4 Discussion

It is well known that the presence of the stent struts within an artery results in unfavorable local hemodynamic conditions [27], potentially promoting inflammatory-related responses such as neointimal hyperplasia especially during the first weeks after stent deployment, which can result in ISR [18,28]. Indeed, a cascade of events based on inflammation and cellular proliferation is commenced within 1-3 days after stenting, with known remodeling phase exponentially increasing starting from the third week after stent implantation [18,29]. Previous evidences on the impact of stent design on WSS patterns by computational, experimental and clinical studies, although performed mainly in coronary arteries, motivates the current investigation [18,30–32]. Specifically, in this work, CFD simulations were performed to investigate the impact of different SFA stent designs on the WSS patterns of a patient-specific SFA anatomy. Three common laser-cut stents (i.e. EverFlex, Zilver, S.M.A.R.T.) and a prototype braided stent were compared by quantifying several WSS-based descriptors. The results of the work showed that the main differences in terms of local hemodynamics were found between the

25

two types of stent design, namely the laser-cut and braided one. In particular, the braided stent was characterized by lower median values of transWSS and higher median values of WSS_{RATIO} than the three laser-cut stents. This suggests that the one-over-one braid pattern of the braided stent mainly impacts the multidirectional WSS vector field, as captured by the transWSS and WSS_{RATIO}, without severely influencing the WSS magnitude. In general, despite the statistical differences found between each distribution, the laser-cut stents presented similar median values of each WSS-based descriptor. The only exception was the Zilver stent, for which the median TAWSS was ~30% higher than that of the EverFlex and S.M.A.R.T. stents (and also of the braided stent). This difference is attributable to the larger cell area that characterize the Zilver stent design as compared to the others, providing a greater luminal area of flow reattachment between the struts [33]. On the basis of these considerations, overall the Zilver stent induced the most favorable local hemodynamic condition, at least when considering the WSS magnitude.

In addition to the stent design, CFD simulations were carried out to investigate the impact of stent overlapping on the hemodynamics of a patient-specific SFA model. From the clinical viewpoint, the best approach to treat long SFA lesions remains to be investigated and a definitive consensus on the optimal endovascular treatment and number of stents to be implanted is yet not available. On the one hand, following a standardized recanalization technique for the Zilver stent [34], in order to properly cover a dilated arterial segment, a minimum stent overlapping region of 5-10 mm was suggested. On the other hand, for long SFA lesions (>100 mm) a single long stent strategy was reported to present a larger mid-term patency as compared to a multiple stenting strategy [35], suggesting stent overlapping as one of the main causes of severe ISR. To the authors' knowledge, this is the first work in which the hemodynamic impact of the order of stent implantation and the overlapping length has been analyzed in SFA models. The findings of the work showed that the presence of stent overlapping provokes an abrupt alteration in the WSS-

26

based descriptors. In particular, lower median values of TAWSS were found at the overlapping region, in agreement with previous investigations on overlapped coronary stents [30–32]. Moreover, the overlapping region exhibited lower median values of transWSS, and higher median values of OSI and WSS_{RATIO} than the stented regions upstream and downstream from the overlapping. Finally, by comparing three configurations of stent implantation (i.e. step-down and step-up, with opposite order of stent implantation, and long-overlap, with longer overlapping length), it was found that the overlapping length, rather than the order of stent implantation, highly and negatively impacts the local hemodynamics. This finding suggests that a shorter overlapping length, if not avoidable, should be preferred from a hemodynamic viewpoint, supporting previous clinical observations [35].

To conduct the CFD simulations in the patient-specific SFA models, an *ad hoc* virtual stent implantation technique based on mesh morphing was here developed to obtain the stented fluid domains. This technique allowed overcoming two main drawbacks that characterize the imaging of diseased SFAs by CT and limit the reconstruction of stented vessels. First, pre-operative CT images with patent SFA lumen are often not available (as in this work) because of the frequent total arterial blockage highly limiting the flowing of the contrast agent. Hence, the pre-operative vessel geometry cannot be reconstructed and a sequential approach based on the virtual deployment of the stent through a finite element analysis followed by the CFD simulation [31] cannot be used. Second, the low resolution of CT and the metallic artefacts caused by the stent in the post-operative CT images do not allow visualizing the stent struts and thus directly reconstructing a 3D model of the stent. To overcome these drawbacks, the proposed technique uses the post-operative SFA lumen geometry and takes advantage of the stent markers clearly visible by CT to correctly position the single or multiple stent models. The procedure is highly efficient as compared to the traditional finite element analyses of stent deployment (e.g. [36,37]),

27

enabling the placement of long stents without the need for high-performance computing resources.

This work is not exempt from limitations. As previously mentioned, the low CT resolution and the presence of metallic artefacts in the CT images impeded the identification of regions of stent malapposition, which were neglected. The visualization of malapposed regions could be significantly improved with the use of intravascular imaging techniques [38], although scarcely employed in analyzing post-treated SFAs. Furthermore, the relative positioning of the stent far from the edge markers and with respect to the other stent in case of virtual implantation of two devices could not be validated through the CT scans, due to the metallic artefacts. The CFD simulations were conducted by considering rigid and fixed walls, thus neglecting the effects of the leg movement on the hemodynamics. In the future, moving-boundary CFD simulations could be carried out to simulate the entire gait cycle by adapting the computational workflow proposed by Colombo et al. [39] for healthy, idealized femoropopliteal models to patient-specific stented SFA models. Even though the averaged flow conditions led to laminar conditions, the occurrence of a transitional flow regime at peak systole in realistic SFA anatomies should be further investigated. Finally, the effect of stent design and stent overlapping on hemodynamics was quantified through the post-processing of the CFD results. However, the knowledge of the impact of the altered local hemodynamics on the biological processes is still insufficient to drive ultimate conclusions on the real biomechanical events that occur and on their contribution to the insurgence of pathologies such as ISR.

5 Conclusions

The computational framework presented in this work allowed comparing different stent designs and stent overlapping configurations from the hemodynamic viewpoint, through the virtual implantation of stents in patient-specific, post-operative models of human SFA reconstructed from CT. The study revealed that the main differences in terms of local hemodynamics, quantified through several WSS-based descriptors, were present between the two main types of SFA self-expanding stent designs, namely the laser-cut versus the braided stents. Alongside, the study proved the importance of limiting the stent overlapping in order to avoid further unfavorable local hemodynamic condition, suggesting that shorter overlapping should always be preferred from the hemodynamic viewpoint, regardless the order of stent implantation.

Acknoledgements

Conflict of interest

The authors declare that the research was conducted in the absence of any commercial or financial relationships that could be construed as a potential conflict of interest.

Authors' contribution

Conceptualization: MC, AC, CC; Data Curation: MC, ACol, GA; Stent modeling: MC, AC, ACol, GA, MB, CMcK, TV; Virtual stenting methodology: MC, AC, ACol, GA, CC; CFD Simulations: MC; Statistical Analyses: MC; Funding Acquisition: CC, FM; Supervision: SB, FM, CC; Writing – Original Draft Preparation: MC, DG, CC; Writing – Review & Editing: MC, AC, DG, ACol, GA, MB, CMcK, SB, TV, FM, CC. All authors discussed the results and reviewed the manuscript.

References

[1]   F.G.R. Fowkes, V. Aboyans, F.J.I. Fowkes, M.M. McDermott, U.K.A. Sampson, M.H. Criqui, Peripheral artery disease: epidemiology and global perspectives, Nat. Rev. Cardiol. 14 (2016) 156–170. https://doi.org/10.1038/nrcardio.2016.179.

[2]   A. Shaker, A. Rahim, O. El Kashef, A. Gad, Balloon angioplasty versus stenting of sequential tandem lesions in superficial femoral and popliteal arteries, Egypt. J. Surg. 35 (2016) 59. https://doi.org/10.4103/1110-1121.176819.

[3]   K. Katsanos, G. Tepe, D. Tsetis, F. Fanelli, Standards of practice for superficial femoral and popliteal artery angioplasty and stenting, Cardiovasc. Intervent. Radiol. 37 (2014) 592–603. https://doi.org/10.1007/s00270-014-0876-3.

[4]   C.G. McKenna, T.J. Vaughan, A finite element investigation on design parameters of bare and polymer-covered self-expanding wire braided stents, J. Mech. Behav. Biomed. Mater. 115 (2021) 104305. https://doi.org/10.1016/j.jmbbm.2020.104305.

[5]   C.G. McKenna, T.J. Vaughan, A Computational Framework Examining the Mechanical Behaviour of Bare and Polymer-Covered Self-Expanding Laser-Cut Stents, Cardiovasc.

Eng. Technol. (2021). https://doi.org/10.1007/s13239-021-00597-w.

[6]   E.J. Armstrong, H. Saeed, B. Alvandi, S. Singh, G.D. Singh, K.K. Yeo, D. Anderson, G.G. Westin, D.L. Dawson, W.C. Pevec, J.R. Laird, Nitinol self-expanding stents vs. balloon angioplasty for very long femoropopliteal lesions, J. Endovasc. Ther. 21 (2014) 34–43. https://doi.org/10.1583/13-4399MR.1.

[7]   S. Banerjee, Superficial femoral artery is not left anterior descending artery, Circulation. 134 (2016) 901–903. https://doi.org/10.1161/CIRCULATIONAHA.116.023690.

[8]   L. Räber, P. Jüni, L. Löffel, S. Wandel, S. Cook, P. Wenaweser, M. Togni, R. Vogel, C. Seiler, F. Eberli, T. Lüscher, B. Meier, S. Windecker, Impact of stent overlap on angiographic and long-term clinical outcome in patients undergoing drug-eluting stent implantation, J. Am. Coll. Cardiol. 55 (2010) 1178–1188. https://doi.org/10.1016/j.jacc.2009.11.052.

[9]   D. Scheinert, S. Scheinert, J. Sax, C. Piorkowski, S. Bräunlich, M. Ulrich, G. Biamino, A. Schmidt, Prevalence and clinical impact of stent fractures after femoropopliteal stenting, J. Am. Coll. Cardiol. 45 (2005) 312–315. https://doi.org/10.1016/j.jacc.2004.11.026.

[10]   J.A. Rymer, W. Schuyler Jones, Femoropopliteal in-stent restenosis: What is the standard of care?, Circ. Cardiovasc. Interv. 11 (2018) 1–10. https://doi.org/10.1161/CIRCINTERVENTIONS.118.007559.

[11]   N.A. Scott, Restenosis following implantation of bare metal coronary stents: Pathophysiology and pathways involved in the vascular response to injury, Adv. Drug Deliv. Rev. 58 (2006) 358–376. https://doi.org/10.1016/j.addr.2006.01.015.

[12]   Y.S. Chatzizisis, A.U. Coskun, M. Jonas, E.R. Edelman, C.L. Feldman, P.H. Stone, Role of endothelial shear stress in the natural history of coronary atherosclerosis and vascular remodeling. molecular, cellular, and vascular behavior, J. Am. Coll. Cardiol. 49 (2007)

2379–2393. https://doi.org/10.1016/j.jacc.2007.02.059.

[13] C. Cheng, D. Tempel, R. Van Haperen, A. Van Der Baan, F. Grosveld, M.J.A.P. Daemen, R. Krams, R. De Crom, Atherosclerotic lesion size and vulnerability are determined by patterns of fluid shear stress, Circulation. 113 (2006) 2744–2753. https://doi.org/10.1161/CIRCULATIONAHA.105.590018.

[14] C. Chiastra, G. Dubini, F. Migliavacca, Hemodynamic perturbations due to the presence of stents, in: Biomech. Coron. Atheroscler. Plaque, Elsevier, 2021: pp. 251–271. https://doi.org/10.1016/b978-0-12-817195-0.00011-1.

[15] C. Gökgöl, N. Diehm, L. Räber, P. Büchler, Prediction of restenosis based on hemodynamical markers in revascularized femoro-popliteal arteries during leg flexion, Biomech. Model. Mechanobiol. 18 (2019) 1883–1893. https://doi.org/10.1007/s10237-019-01183-9.

[16] M. Colombo, Y. He, A. Corti, D. Gallo, S. Casarin, J.M. Rozowsky, F. Migliavacca, S. Berceli, C. Chiastra, Baseline local hemodynamics as predictor of lumen remodeling at 1-year follow-up in stented superficial femoral arteries, Sci. Rep. 11 (2021) 1–13. https://doi.org/10.1038/s41598-020-80681-8.

[17] M. Colombo, Y. He, A. Corti, D. Gallo, F. Ninno, S. Casarin, J.M. Rozowsky, F. Migliavacca, S. Berceli, C. Chiastra, In-stent restenosis progression in human superficial femoral arteries: dynamics of lumen remodeling and impact of local hemodynamics, Ann. Biomed. Eng. 49 (2021) 2349–2364. https://doi.org/10.1007/s10439-021-02776-1.

[18] K.C. Koskinas, Y.S. Chatzizisis, A.P. Antoniadis, G.D. Giannoglou, Role of endothelial shear stress in stent restenosis and thrombosis: Pathophysiologic mechanisms and implications for clinical translation, J. Am. Coll. Cardiol. 59 (2012) 1337–1349. https://doi.org/10.1016/j.jacc.2011.10.903.

[19]   M. Colombo, M. Bologna, M. Garbey, S. Berceli, Y. He, J.F. Rodriguez Matas, F. Migliavacca, C. Chiastra, Computing patient-specific hemodynamics in stented femoral artery models obtained from computed tomography using a validated 3D reconstruction method, Med. Eng. Phys. 75 (2020) 23–35. https://doi.org/10.1016/j.medengphy.2019.10.005.

[20]   C.G. McKenna, T.J. Vaughan, An experimental evaluation of the mechanics of bare and polymer-covered self-expanding wire braided stents, J. Mech. Behav. Biomed. Mater. 103 (2020) 103549. https://doi.org/10.1016/j.jmbbm.2019.103549.

[21]   R. Ponzini, C. Vergara, A. Redaelli, A. Veneziani, Reliable CFD-based estimation of flow rate in haemodynamics measures, Ultrasound Med. Biol. 32 (2006) 1545–1555. https://doi.org/10.1016/j.ultrasmedbio.2006.05.022.

[22]   D.N. Ku, D.P. Giddens, C.K. Zarins, S. Glagov, Pulsatile flow and atherosclerosis in the human carotid bifurcation. Positive correlation between plaque location and low oscillating shear stress, Arterioscler. Thromb. Vasc. Biol. 5 (1985) 293–302. https://doi.org/10.1161/01.ATV.5.3.293.

[23]   H.A. Himburg, D.M. Grzybowski, A.L. Hazel, J.A. LaMack, X.M. Li, M.H. Friedman, Spatial comparison between wall shear stress measures and porcine arterial endothelial permeability, Am J Physiol Hear. Circ Physiol. 286 (2004) H1916-22. https://doi.org/10.1152/ajpheart.00897.2003.

[24]   Y. Mohamied, S.J. Sherwin, P.D. Weinberg, Understanding the fluid mechanics behind transverse wall shear stress, J. Biomech. 50 (2017) 102–109. https://doi.org/10.1016/j.jbiomech.2016.11.035.

[25]   U. Morbiducci, D. Gallo, S. Cristofanelli, R. Ponzini, M.A. Deriu, G. Rizzo, D.A. Steinman, A rational approach to defining principal axes of multidirectional wall shear

33

stress in realistic vascular geometries, with application to the study of the influence of helical flow on wall shear stress directionality in aorta, J. Biomech. 48 (2015) 899–906. https://doi.org/10.1016/j.jbiomech.2015.02.027.

[26]   I. Tarrahi, M. Colombo, E.M.J. Hartman, M.N.T. Forero, R. Torii, C. Chiastra, J. Daemen, F.J.H. Gijsen, Impact of bioresorbable scaffold design characteristics on local haemodynamic forces: An ex vivo assessment with computational fluid dynamics simulations, EuroIntervention. 16 (2020) E930–E937. https://doi.org/10.4244/EIJ-D-19-00657.

[27]   C. Chiastra, G. Dubini, F. Migliavacca, Hemodynamic perturbations due to the presence of stents, in: Biomech. Coron. Atheroscler. Plaque, Elsevier, 2021: pp. 251–271. https://doi.org/10.1016/B978-0-12-817195-0.00011-1.

[28]   E. Kokkalis, N. Aristokleous, J.G. Houston, Haemodynamics and Flow Modification Stents for Peripheral Arterial Disease: A Review, Ann. Biomed. Eng. 44 (2016) 466–476. https://doi.org/10.1007/s10439-015-1483-4.

[29]   E.R. Edelman, C. Rogers, Pathobiologic responses to stenting, Am. J. Cardiol. 81 (1998) 4E-6E. https://doi.org/10.1016/S0002-9149(98)00189-1.

[30]   F. Rikhtegar, C. Wyss, K.S. Stok, D. Poulikakos, R. Müller, V. Kurtcuoglu, Hemodynamics in coronary arteries with overlapping stents, J. Biomech. 47 (2014) 505–511. https://doi.org/10.1016/j.jbiomech.2013.10.048.

[31]   C. Chiastra, S. Morlacchi, D. Gallo, U. Morbiducci, R. Cardenes, I. Larrabide, F. Migliavacca, Computational fluid dynamic simulations of image-based stented coronary bifurcation models, J. R. Soc. Interface. 10 (2013) 20130193. https://doi.org/10.1098/rsif.2013.0193.

[32]   M. Lagache, R. Coppel, G. Finet, F. Derimay, R.I. Pettigrew, J. Ohayon, M. Malvè,

Impact of malapposed and overlapping stents on hemodynamics: A 2d parametric computational fluid dynamics study, Mathematics. 9 (2021) 795. https://doi.org/10.3390/math9080795.

[33]　T.J. Gundert, A.L. Marsden, W. Yang, J.F. LaDisa, Optimization of Cardiovascular Stent Design Using Computational Fluid Dynamics, J. Biomech. Eng. 134 (2012) 011002. https://doi.org/10.1115/1.4005542.

[34]　M. Ferreira, L. Lanziotti, M. Monteiro, G. Abuhadba, L.F. Capotorto, L. Nolte, N. Fearnot, Superficial femoral artery recanalization with self-expanding nitinol stents: long-term follow-up results., Eur. J. Vasc. Endovasc. Surg. 34 (2007) 702–8. https://doi.org/10.1016/j.ejvs.2007.07.025.

[35]　U. Bildirici, M. Aktas, E. Dervis, U. Çelikyurt, Mid-term outcomes of stent overlap in long total occluded lesions of superficial femoral artery, Med. Sci. Monit. 23 (2017) 3130–3134. https://doi.org/10.12659/MSM.902413.

[36]　C. Gökgöl, N. Diehm, F.R. Nezami, P. Büchler, Nitinol stent oversizing in patients undergoing popliteal artery revascularization: a finite element study, Ann. Biomed. Eng. 43 (2015) 2868–2880. https://doi.org/10.1007/s10439-015-1358-8.

[37]　P. Mortier, J.J. Wentzel, G. De Santis, C. Chiastra, F. Migliavacca, M. De Beule, Y. Louvard, G. Dubini, Patient-specific computer modelling of coronary bifurcation stenting: The John Doe programme, EuroIntervention. 11 (2015) V35–V39. https://doi.org/10.4244/EIJV11SVA8.

[38]　C. Gökgöl, Y. Ueki, D. Abler, N. Diehm, R.P. Engelberger, T. Otsuka, L. Räber, P. Büchler, Towards a better understanding of the posttreatment hemodynamic behaviors in femoropopliteal arteries through personalized computational models based on OCT images, Sci. Rep. 11 (2021) 1–12. https://doi.org/10.1038/s41598-021-96030-2.

[39]   M. Colombo, G. Luraghi, L. Cestariolo, M. Ravasi, A. Airoldi, C. Chiastra, G. Pennati,

Impact of lower limb movement on the hemodynamics of femoropopliteal arteries: A

computational study, Med. Eng. Phys. 81 (2020) 105–117.

https://doi.org/10.1016/j.medengphy.2020.05.004.